Combined Lidar-Radar Remote Sensing: Initial Results from CRYSTAL-FACE and Implications for Future Spaceflight Missions

M.J. McGill, L. Li, W.D. Hart, G.M. Heymsfield, D.L. Hlavka,

M.A. Vaughan, and D.M. Winker

Dr. Matthew J. McGill
NASA Goddard Space Flight Center, Code 912
Greenbelt, MD 20771
phone: 301-614-6281
fax: 301-614-5492
email: matthew.j.mcgill@nasa.gov

Dr. Lihua Li
NASA Goddard Space Flight Center, Code 912
Greenbelt, MD 20771
phone: 301-614-6356
fax: 301-614-5492
email: lihua@agnes.gsfc.nasa.gov

Mr. William D. Hart
Science Systems and Applications, Inc.
NASA Goddard Space Flight Center, Code 912
Greenbelt, MD 20771
phone: 301-614-6272
fax: 301-614-5492
email: billhart@virl.gsfc.nasa.gov

Dr. Gerald M. Heymsfield
Science Systems and Applications, Inc.
NASA Goddard Space Flight Center, Code 912
Greenbelt, MD 20771
phone: 301-614-6369
fax: 301-614-5492
email: gerald.heymsfield@nasa.gov

Mr. Dennis L. Hlavka
Science Systems and Applications, Inc.
NASA Goddard Space Flight Center, Code 912
Greenbelt, MD 20771
phone: 301-614-6278
fax: 301-614-5492
email: sgdlh@virl.gsfc.nasa.gov

Mr. Mark A. Vaughan
Science Applications International Corp.
NASA Langley Research Center, Code 435
Hampton, VA 23681
phone: 757-864-5331
fax: 757-864-7775
email: m.a.vaughan@larc.nasa.gov

Dr. David M. Winker
NASA Langley Research Center, Code 435
Hampton, VA 23681
phone: 757-864-6747
fax: 757-864-7775
email: david.m.winker@nasa.gov

Submitted to Journal of Geophysical Research

July, 2003

Popular Summary

Combined Lidar-Radar Remote Sensing: Initial Results from CRYSTAL-FACE and Implications for Future Spaceflight Missions

M.J. McGill, L. Li, W.D. Hart, G.M. Heymsfield,
D.L. Hlavka, M.A. Vaughan, and D.M. Winker

In the near future NASA plans to fly satellites carrying a multi-wavelength backscatter lidar and a 94-Ghz cloud profiling radar in formation to provide complete global profiling of cloud and aerosol properties. The Cirrus Regional Study of Tropical Anvils and Cirrus Layers - Florida Area Cirrus Experiment (CRYSTAL-FACE) field campaign, conducted during July 2002, provided the first high-altitude colocated measurements from lidar and cloud profiling radar to simulate these spaceborne sensors. The lidar and radar provide complementary measurements with varying degrees of measurement overlap. This paper presents initial results of the combined airborne lidar-radar measurements during CRSYTAL-FACE. The overlap of instrument sensitivity is presented, within the context of particular CRYSTAL-FACE conditions. Results are presented to quantify the portion of atmospheric profiles sensed independently by each instrument and the portion sensed simultaneously by the two instruments.

ABSTRACT

In the near future NASA plans to fly satellites carrying a multi-wavelength backscatter lidar and a 94-GHz cloud profiling radar in formation to provide complete global profiling of cloud and aerosol properties. The CRYSTAL-FACE field campaign, conducted during July 2002, provided the first high-altitude colocated measurements from lidar and cloud profiling radar to simulate these spaceborne sensors. The lidar and radar provide complementary measurements with varying degrees of measurement overlap. This paper presents initial results of the combined airborne lidar-radar measurements during CRSYTAL-FACE. The overlap of instrument sensitivity is presented, within the context of particular CRYSTAL-FACE conditions. Results are presented to quantify the portion of atmospheric profiles sensed independently by each instrument and the portion sensed simultaneously by the two instruments.

INTRODUCTION

A series of satellites, flying in formation and providing synergistic data products, comprise NASA's future "A-train" constellation. The A-train takes its name from the Aqua satellite [Parkinson, 2003], which leads the string of satellites. Following Aqua are, in order, the CloudSat [Stephens *et al*, 2002], CALIPSO [Winker *et al*, 2003], PARASOL carrying the POLDER instrument [Deschamps *et al*, 1994], and Aura[ref] satellites. These satellites will fly in a 705-km sun-synchronous orbit with an equatorial crossing time of 1:30 pm. This satellite formation offers the opportunity to combine complementary data products to provide improved global remote sensing of the atmosphere.

The Cirrus Regional Study of Tropical Anvils and Cirrus Layers - Florida Area Cirrus Experiment (CRYSTAL-FACE) field campaign during July 2002 [Jensen *et al*, 2003] deployed a comprehensive suite of instruments on six aircraft and at two ground sites to study tropical cirrus cloud properties and formation processes. Instruments onboard one of the aircraft, the NASA ER-2, provided high-altitude downlooking measurements from several instruments that can be considered proxies for A-train instruments. The Cloud Physics Lidar (CPL) [McGill *et al*, 2002; McGill *et al*, 2003] provides measurements similar to the polarization lidar on CALIPSO, which operates at 532 nm and 1064 nm. The new Cloud Radar System (CRS) [Li *et al*, 2003] provides measurements similar of those of the CloudSat 94 GHz cloud profiling radar. The MODIS Airborne Simulator (MAS) [King *et al*, 1996] emulates MODIS measurements of the Aqua satellite.

This work will focus on selected CPL and CRS measurements from CRYSTAL-FACE, as these are the first high-altitude, colocated measurements from lidar and cloud profiling radar and can be used to assess the utility of future data products from CALIPSO and CloudSat. The combination of the two instruments, with wavelengths that differ by about three orders of magnitude, is necessary to obtain a complete profile of clouds and aerosols. The radar is insensitive to aerosols and to clouds composed of small particles, but is very sensitive to clouds composed of large ice crystals and can easily penetrate dense convective cloud. In contrast, lidar is sensitive to aerosols and to even the thinnest cloud layers, but cannot penetrate optically thick clouds. Because of its use of optical wavelengths, lidar is usually limited to situations where the integral optical depth is less than ~3-4, depending on instrument parameters. Similarities and differences in using the two techniques to remotely sense clouds will be illustrated using data

acquired during CRYSTAL-FACE on July 23 and July 26, 2002. The data acquired on July 23 represent unique measurements of a developing cirrus anvil, while on July 26 primarily non-convective cirrus was observed.

COMBINED LIDAR-RADAR OBSERVATIONS

The CPL provides measurements with 30 m vertical by 1 s temporal resolution. At an average ER-2 ground speed of ~200 m/s the corresponding horizontal resolution is approximately 200 m. The CRS measurements are 37.5 m vertical by 0.5 s temporal resolution. Thus, the first step in combining the CPL and CRS data is to match the spatial and temporal resolutions of the two data sets. For ease of computation, we chose to interpolate the CPL measurements to 37.5 m vertical resolution and to average the CRS measurements to 1 s temporal resolution. The CPL measures at both 532 nm and 1064 nm. However, only 532 nm data is used in this paper. The 1064 nm data is not much different, and either lidar wavelength is greatly separated from the millimeter radar wavelength.

There are difficulties involved in combining data from lidar and radar, not the least of which is a fundamental difference in measured quantities. Whereas the lidar measures backscattered photons, or equivalently, profiles of attenuated backscatter, the radar measurement is quantified in terms of equivalent reflectivity. Thus, one aspect of this work is to relate the radar reflectivity to lidar-derived quantities such as backscatter and optical depth. A most important distinction between lidar and radar is the reliance on particle size distribution. Reflectivity of the millimeter-wave radar is proportional to the sixth power of the particle size distribution, whereas

lidar backscatter is proportional to the second power. A comprehensive introduction to lidar and radar is beyond the scope of this paper, but an excellent reference (coincidentally focused on CloudSat and CALIPSO measurement synergy) is Okamoto *et al.* (2003).

Difficulties also arise when combining data from two separate sensors. In this case, many of the usual problems are remedied by having both CPL and CRS onboard the same aircraft. However, concerns such as pointing and footprint sizes are always present. Radar beam footprints are usually large compared with lidar, and that is the case here as well. The CPL receiver field of view is 100 microradians, so the receiver footprint at 20 km is 2 m. The CRS has a pencil beam but aircraft motion over the averaging interval elongates the footprint; at 20 km altitude the footprint is approximately 200 x 280 m. Although no attempt was made to precisely co-align the CPL and CRS, the disparity in footprint size provides wide margin in the pointing requirement. The difference in footprint, however, introduces the reality that the lidar essentially subsamples the area sampled by the radar. Thus, small features, such as fair weather cumulus clouds with few hundred meter diameters, might be detected by the lidar but not by the radar.

Initial focus for this study is the July 23 case from CRYSTAL-FACE because the ER-2 flew 8 passes along the same coordinates. The flight track, shown in Figure 1, was chosen to follow a developing convective cell and was intentionally chosen in the along-wind direction. The result is a unique data set showing growth and decay of the cirrus anvil over the course of a nearly 4-hour period. This particular data set provides a good basis for combining lidar and radar data due to the range of conditions observed, including thick convective clouds, thin cirrus, and multiple cloud layering.

The right-hand column in Figure 2 shows the CPL data from the eight flight tracks. The data are plotted such that the images have common latitude-longitude end points even if the data does not extend to the end point. By plotting the data in this manner, it is easy to see the evolution of the convective system on a fixed latitude-longitude grid. In addition, every other image is plotted in reverse of the normal time scale to allow viewing on the fixed grid. In the first image two neighboring convective cells are seen, with a cirrus anvil starting to form. In successive images the convective cells collapse and decay while the cirrus anvil spreads downstream and decays into a complex multi-layered structure.

Figure 3 shows the CRS data in the left-hand column. Note the convective core is easily observed by the radar whereas the lidar could not penetrate far into the layer. Conversely, the radar is oblivious to much of the thin cirrus, even layers that are geometrically thick, which the lidar easily senses. This is particularly apparent in the bottom three panels of Figure 3 between 12 km and 13.5 km, where the radar fails to detect all but a small fraction of the uppermost cirrus layer. The right-hand column of Figure 3 shows the combined atmosphere generated from both CRS and CPL data. In these images yellow shading indicates regions where only the radar observed layers, blue shading indicates regions where only the lidar observed layers, and green shading is where both instruments observed layers. Figure 3 thus provides a qualitative but visual overview of the instrument sensitivities and overlap between the measurements. The combined lidar-radar images provide a first glimpse of the future CALIPSO-CloudSat combined data product.

LIDAR-RADAR OBSERVATIONS: QUANTITATIVE RESULTS

Providing absolute comparisons of the lidar and radar measurements is difficult. A significant complication in comparing measurements from simple backscatter lidar and radar is that neither instrument is capable of directly measuring particle size and shape. Thus, there are three large degrees of freedom in the atmospheric particulates (particle size, particle shape, and concentration) that affect each instrument in different ways. In particular, lidar is sensitive to equivalent particle diameter squared while radar is sensitive to equivalent particle diameter to the sixth power. And, although lidar depolarization measurements (which are obtained by the CPL) might be used to aid in comparing the lidar and radar data, such measurements are not unambiguous, since particle size and orientation can vary independently.

Before beginning detailed descriptions of the data, it is necessary to define some terminology. Because the radar signal does not incur significant attenuation and can penetrate most, if not all, atmospheric cloud features, the radar data can be partitioned into two basic categories: (1) that within layers (e.g., cloud) and (2) clear air. For this work, radar cloud boundaries were determined using a thresholding technique similar to that described in Uttal *et al.* (1993). The lidar signal, however, can become completely extinguished when attempting to probe a dense cloud, so the lidar data is best partitioned into three categories: (1) that within layers, which for the lidar can be cloud, elevated aerosol or planetary boundary layer, (2) clear air, and (3) totally attenuated regions (e.g., the area beneath attenuating clouds). The lidar layer boundaries were also determined using a thresholding technique similar to Winker and Vaughan (1994). Finally, in describing the lidar-derived optical depth, it is understood that the optical depth is that due to

aerosol and cloud and does not include Rayleigh signal (e.g., is particulate rather than total optical depth).

Having established definitions of layers, a description of the observations can now proceed. The 8 flight tracks of July 23, as shown in Figures 2 and 3, consist of a total of over 5 million possible data elements, or data bins (533 bins per profile at a flight altitude of 20 km). The radar detected cloud in 21.9% of the bins and clear air in the remaining 78.1%. From examining the lidar profiles we found that 10.5% of the radar clear air fraction is actually not clear air but contains cloud that was below the radar detection threshold. The lidar detected a layer in 14.8% of the bins, clear air in 26.7%, and was totally attenuated in 58.6% of the bins. From examining the radar data, a lower bound can be determined for the actual cloud fraction contained in regions of lidar data that were totally attenuated. In this case, we find that 25.6% of the totally attenuated bins contained cloud.

Another way to analyze the detection capability of each instrument is to examine only those data bins classified as being within a layer. Using just the data bins within layers, 27.3% were observed by only the lidar while 21.7% were detected by both lidar and radar and 51.0% were detected by only the radar. These statistics are summarized in Table 1. In this particular case, the complementary nature of the measurements is evident and there is a good degree of overlap between the instruments.

Table 1: Statistics from July 23 and July 26 cases.

	July 23	**July 26**
total number of profiles used	8927	13761
total number of possible data elements (bins)	5,000,719	7,373,469
radar: % total bins with data in layers	21.9%	2.5%
radar: % total bins in clear air	78.1%	97.5%
lidar: % total bins with data in layers	14.8%	7.4%
lidar: % total bins in clear air	26.7%	81.8%
lidar: % total bins fully attenuated	58.6%	10.8%
% bins detected by lidar only (within layers)	27.3%	72.4%
% bins detected by both lidar and radar (within layers)	21.7%	9.5%
% bins detected by radar only (within layers)	51.0%	18.2%

To quantify the lidar-radar vertical overlap, two particular profiles were selected from the third image segment in Figure 3 (indicated by vertical red lines on the image). Figure 4 shows a profile from 20:38:20 UTC, for a case where a transmissive cirrus cloud is found. In this example, the lidar detects two separate cirrus layers and penetrates through both (ground return is observed beneath). The radar does not detect the top cirrus layer, but does detect the lower portion of the second layer. The lidar cumulative aerosol optical depth reaches 0.25 before the

radar begins to detect signal at its lowest sensitivity. Figure 5 shows a profile from 20:50:50 UTC, but in this example the lidar signal is quickly attenuated by the dense clouds. Although the lidar detects the cirrus top before the radar does, the lidar signal is fully extinguished by 13 km. The lidar cumulative aerosol optical depth has reached 0.15 before the radar signature begins. Figures 4 and 5 illustrate the complementary nature of the lidar and radar measurements, with the radar penetrating where the lidar cannot and the lidar sensitivity permitting observation of thin cirrus invisible to the radar.

Analysis of many such profiles permits development of a relationship between lidar optical depth and radar minimum reflectivity. Figure 6 shows relationship between the topmost layer boundary determined from the radar and lidar data. In general the lidar detects the topmost layer boundary (i.e., that closest to the aircraft) before the radar does, in many cases more than 1 km higher. Thus, there is often a region of cirrus, which can be geometrically thick, that is undetected by the radar. Because such cirrus are radiatively significant,[McFarquhar *et al.* 2000] the combination of lidar and radar is effective in providing more complete knowledge of the atmospheric column than either instrument alone. Figure 7 is a scatterplot illustrating the relationship between reflectivity and cumulative particulate optical depth. It is apparent that the CRS has a minimum sensitivity of ~-29 dBZ and there is a large amount of scatter owing to large variability in the ice particle characteristics. Figure 8 shows the fraction of occurrences of the lidar cumulative particulate optical depth not seen by the radar. In general, the radar does not start to detect a layer until the lidar cumulative particulate optical depth reaches 0.3-0.4.

It is illuminating to plot the lidar data as a distribution of the observed backscatter coefficient, as shown in Figure 9. Because most of the layers observed are cloud as opposed to elevated aerosol, the histogram skews to higher backscatter coefficients. Overplotted in gray is the subset of lidar backscatter coefficients in regions sensed by both the lidar and the radar. Clearly the radar is most effective in regions with backscatter coefficient greater than $\sim 10^{-5}$ m^{-1} sr^{-1}. Figure 10 is the subset of lidar backscatter coefficients, but only in layers that the radar did not detect, plotted as the fraction of occurrences missed by the radar. Figure 10 demonstrates that the radar is good at detecting layers with large backscatter coefficient ($>10^{-5}$ m^{-1} sr^{-1}) but the lidar is necessary to detect regions with lower backscatter coefficient.

The case from July 23 is obviously specific to cirrus anvils in a tropical tropopause region. It is therefore not possible to make generic statements about the fractional overlap of the lidar and radar measurements for other cloud situations. To emphasize this point, data from July 26 were analyzed in the same manner as July 23. The July 26 flight was a long excursion south to 14 degrees North latitude, as shown in Figure 11. A composite lidar-radar image, similar to the right-hand column of Figure 3, is shown in Figure 12. The lidar detects a thick, extensive cirrus layer as well as elevated Saharan dust above the marine boundary layer. Note the lack of CRS data, even over the geometrically thick cirrus at the southern end of the flight track. In regions that CRS does not detect, CPL estimates of cirrus optical depth are in the range 0.35-0.45 (+/- 0.14) for this cirrus cloud, in line with the CRS detection threshold of 0.3-0.4 determined from the July 23 case. This provides an interesting contrast, because the cirrus anvils from July 23 were comprised of large aggregate ice clusters (as measured by in situ sensors) while the benign synoptic cirrus seen on July 26 is likely comprised of smaller and more geometrically idealized

particles. We may conclude, then, that while the type of cirrus cloud (e.g., particle size and shape) between the two cases is likely quite different, the end result for minimum radar detection is unchanged.

The July 26 data show a definite difference in distribution compared to the July 23 data. Figure 13 shows the comparison of topmost layer boundary (c.f. Figure 6). Figure 14 gives the relation between reflectivity and lidar-derived cumulative particulate optical depth (c.f. Figure 7). The difference is also reflected in the statistics given in Table 1, where the number of data bins within layers detected by the lidar only is more than double that of the July 23 case. A further illustration of the difference between the two cases is shown in Figure 15, which shows the distribution of CRS reflectivity for July 23 and July 26. In the July 23 case, as seen in Figure 3, there is cirrus but also considerable convective cloud. The July 26 case (recall Figure 12) is primarily cirrus with some convective cloud and this fact is evidenced by the reflectivity being clustered in the –20 to –30 dBZ range. For comparison, histograms of the lidar backscatter and that undetected by the radar are shown in Figures 16 and 17 (c.f. Figures 9 and 10). It appears in Figure 17 that the radar misses a large fraction of areas having high backscatter coefficient, but this is merely a reflection of the small number of occurrences (see Figure 16 for context).

CONCLUSIONS

The CRYSTAL-FACE field campaign provided the first high-altitude colocated measurements from lidar and cloud profiling radar. Initial results of the combined lidar-radar measurements were shown, illustrating the complementary nature of the two instruments. Statistics derived

from the measurements demonstrate the sensitivity of each instrument and the region of detection overlap between the instruments. The radar reflectivity was related to lidar-derived parameters such as optical depth. It was determined that cirrus cloud with optical depth <~0.4 is infrequently observed by the radar, but these radiatively significant clouds are easily profiled with the lidar. In contrast, optically thick clouds and convective cores are highly attenuating to lidar but are easily probed with the radar.

Most of the CRYSTAL-FACE flights were focused on convective systems and cirrus anvils. There was, however, one long flight that did not target convective systems. To capture some element of varying atmospheric characteristics, two cases were analyzed, one with convective systems and cirrus anvils and one having synoptic cirrus and considerable clear air. The two cases show quite different results, primarily due to differences in cloud distributions but also presumably because the ice hydrometeors have different characteristics. It follows that the best instrument for providing a complete profile of atmospheric clouds and aerosols is not a lidar or a radar, but a combination of both sensors. The combination of CPL and CRS measurements from CRYSTAL-FACE gives a first glimpse of the combined data product from the future CALIPSO and CloudSat missions and provides a clear indicator of the data synergy that exists between these two remote sensing methods.

ACKNOWLEDGEMENTS

The Cloud Physics Lidar is sponsored by NASA's Radiation Sciences Program (Code YS) and by NASA's Earth Observing System (EOS) office. The Cloud Radar System is sponsored by

NASA's Radiation Sciences Program (Code YS). Data presented was collected as part of the Cirrus Regional Study of Tropical Anvils and Cirrus Layers - Florida Area Cirrus Experiment (CRYSTAL-FACE) field campaign.

REFERENCES

Deschamps, P.Y., F.M. Breon, M. Leroy, A. Podaire, A. Bricaud, J.C. Buriez, and G. Seze, "The POLDER mission: Instrument characteristics and scientific objectives," *IEEE Transactions on Geoscience and Remote Sensing*, **32**, 598-615, 1994.

Jensen, E.J., D.E. Anderson, H.B. Selkirk, D.O. Starr,and O.B. Toon, "Overview of the Cirrus Regional Study of Tropical Anvils and Cirrus Layers – Florida Area Cirrus Experiment (CRYSTAL-FACE)," *Bulletin of the American Meteorological Society*, 2003 (submitted).

King, M.D., W.P. Menzel, P.S. Grant, J.S. Myers, G.T. Arnold, S.E. Platnick, L.E. Gumley, S.C. Tsay, C.C. Moeller, M. Fitzgerald, K.S. Brown, and F.G. Osterwisch, "Airborne scanning spectrometer for remote sensing of cloud, aerosol, water vapor, and surface properties," *Journal of Atmospheric and Oceanic Technology*, **13**, 777-794, 1996.

Li, L., G.M. Heymsfield, P.E. Racette, L. Tian, and E. Zenker, "The 94 Ghz Cloud Radar System on the NASA ER-2 Aircraft," *Journal of Atmospheric and Oceanic Technology*, 2003 (submitted).

McFarquhar, G.M., A.J. Heymsfield, J. Spinhirne, and W. Hart, "Thin and subvisual tropopause tropical cirrus: observations and radiative impacts," *Journal of the Atmospheric Sciences*, **57**, 1841-1853 (2000).

McGill, M.J., D.L. Hlavka, W.D. Hart, V.S. Scott, J.D. Spinhirne, and B. Schmid, "The Cloud Physics Lidar: instrument description and initial measurement results," *Applied Optics*, **41**, 3725-3734, 2002.

McGill, M.J., D.L. Hlavka, W.D. Hart, E.J. Welton, and J.R. Campbell, "Airborne lidar measurements of aerosol optical properties during SAFARI-2000," *Journal of Geophysical Research*, **108**, doi: 10.1029/2002JD002370, 2003.

Okamoto, H., S. Iwasaki, M. Yasui, H. Horie, H. Kuroiwa, and H. Kumagai, "An algorithm for retrieval of cloud microphysics using 95-GHz cloud radar and lidar," *Journal of Geophysical Research*, **108**, doi: 10.1029/2001/JD001225, 2003.

Parkinson, C.L., "Aqua: An Earth-observing satellite mission to examine water and other climate variables," *IEEE Transactions on Geoscience and Remote Sensing*, **41**, 173-183, 2003.

Stephens, G.L., D.G. Vane, R.J. Boain, G.G. Mace, K. Sassen, Z. Wang, A.J. Illingworth, E.J. O'Connor, W.B. Rossow, S.L. Durden, S.D. Miller, R.T. Austin, A. Benedetti, C. Mitrescu, and the CloudSat Science Team, The CloudSat Mission and the A-Train: A New Dimension of

Space-Based Observations of Clouds and Precipitiation, *Bulletin of the American Meteorological Society*, **83**, 1771-1790, 2002.

Uttal, T., L.I. Church, B.E. Martner, and J.S. Gibson, "CLDSTATS: A Cloud Boundary Detection Algorithm for Vertically Pointing Radar Data," NOAA Technical Memorandum ERL WPL-233, Wave Propagation Laboratory, Boulder, CO, July 1993.

Winker, D.M. and M.A. Vaughan, "Vertical distribution of clouds over Hampton, Virginia, observed by lidar under the ECLIPS and FIRE ETO programs," *Atmospheric Research*, **34**, 117-133, 1994.

Winker, D.M., J. Pelon and M.P. McCormick, The CALIPSO Mission: spaceborne lidar for observation of aerosols and clouds, in *Proceedings of SPIE*, Vol. 4893 (U. Singh, T. Itabe, Z. Liu eds.), pp. 1-11, Hangzhou, China, 24-25 October 2002.

FIGURE CAPTIONS

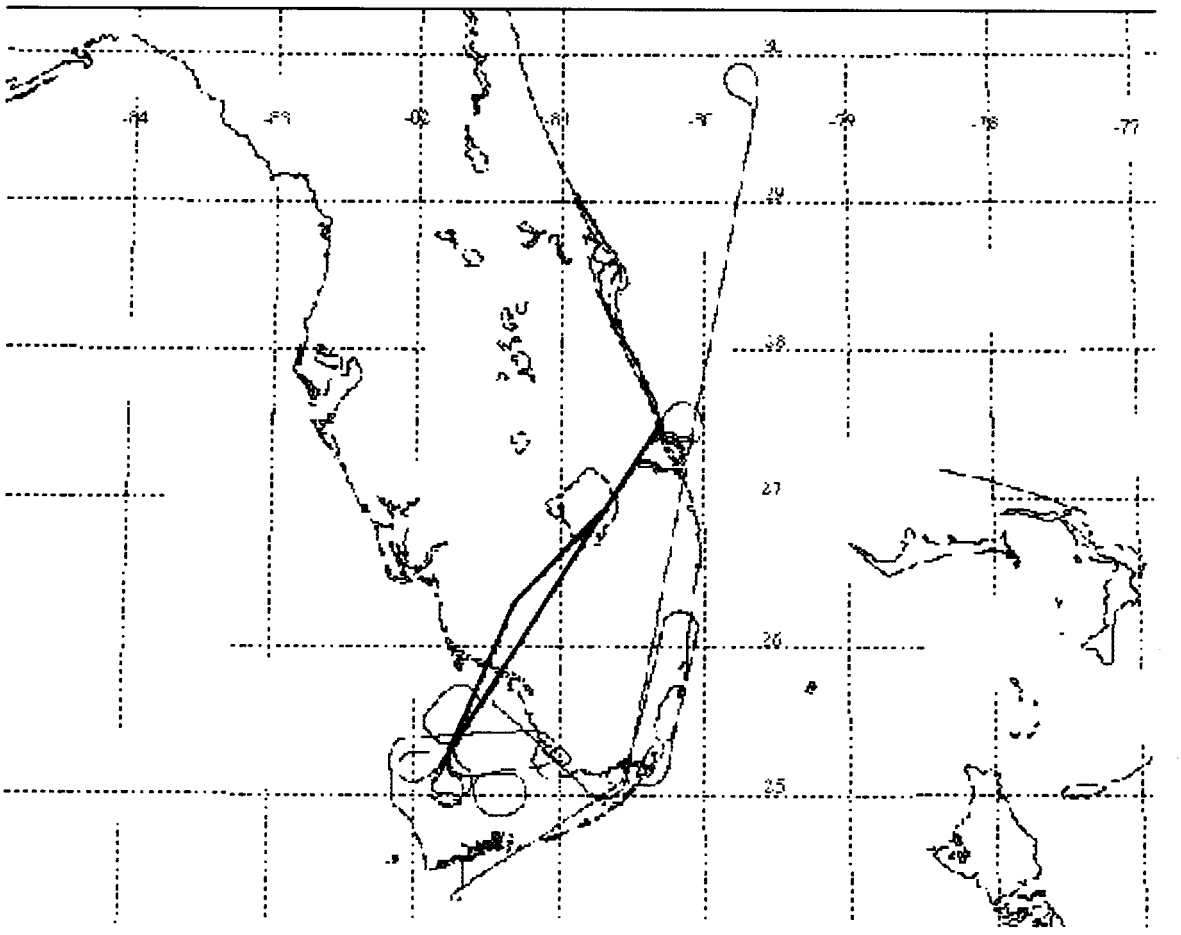

Figure 1: ER-2 flight track for July 23, 2002. Segments drawn in green are the segments shown in Figures 2 and 3.

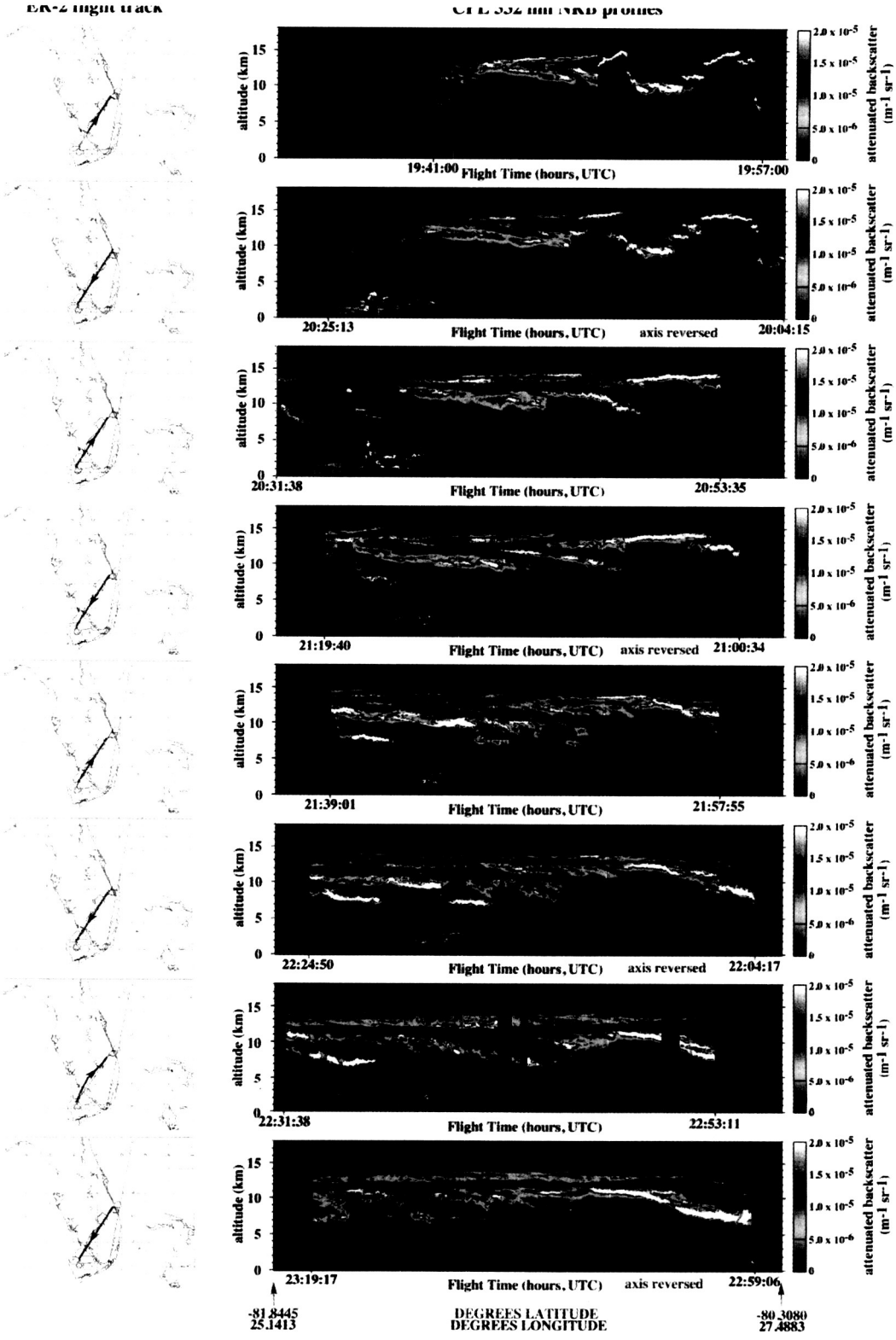

Figure 2: Left-hand column shows ER-2 flight track for each image. Arrows indicate direction of travel. Right-hand column shows profiles of CPL 532 nm attenuated backscatter coefficient. Each image is the same length and covers the same (latitude, longitude) interval. Note that data from westbound flight legs (images 2, 4, 6, 8) has been reversed to allow direct comparison with the eastbound flight legs. Plotted in this manner, it is easy to see evolution of the convective system and anvil in a fixed coordinate system

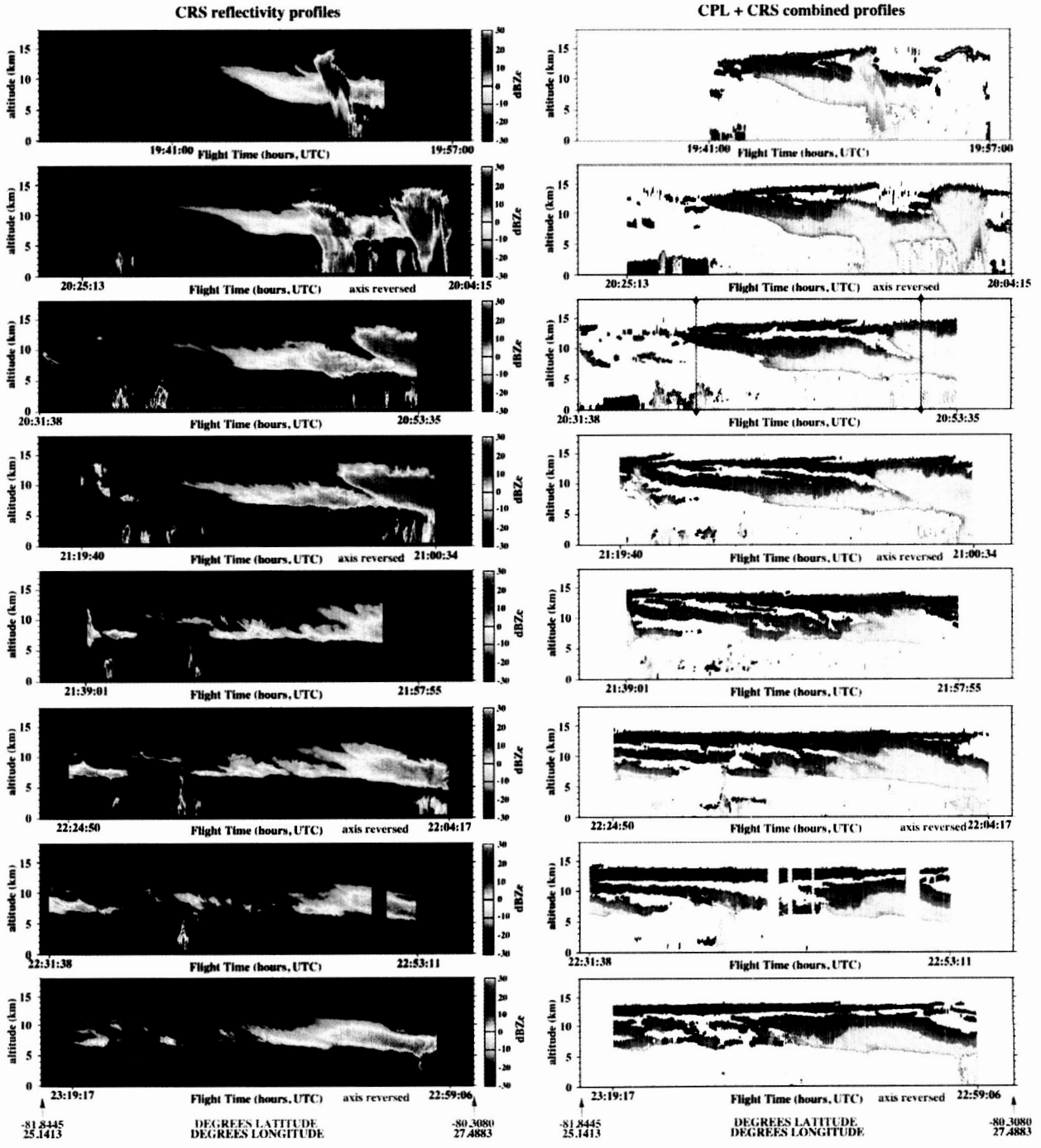

Figure 3: Left-hand column shows profiles of CRS reflectivity. The radar easily penetrates thick clouds but is insensitive to overlying cirrus. Right-hand column is the combined lidar and radar image. Blue color shading indicates regions where only CPL detected layers. Yellow color shading indicates regions where only CRS detected layers. Green shading indicates regions where both CRS and CPL detected layers (e.g., the instrument overlap). These plots show cloud/aerosol layers only (e.g., background atmosphere is removed from the lidar data).

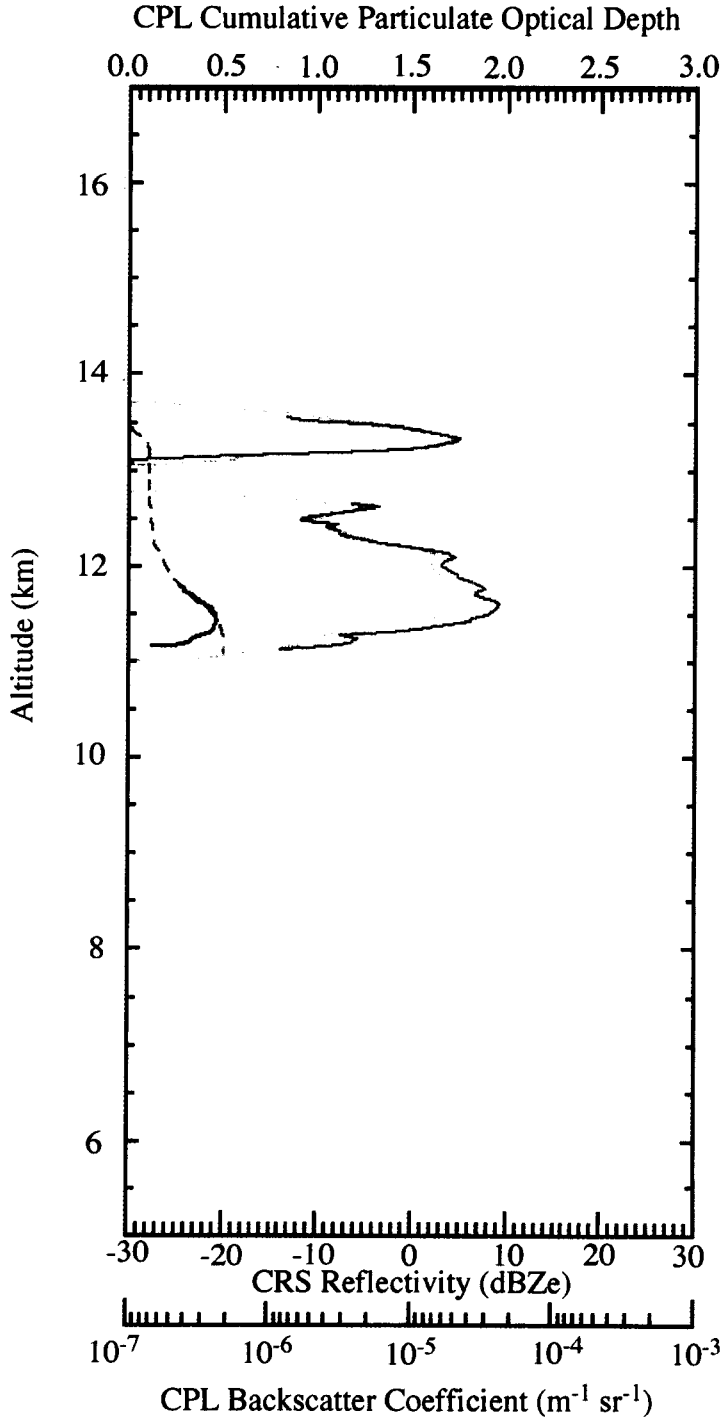

Figure 4: Profiles from 20:30:20 UTC, July 23, 2002. Solid black line is the CRS radar reflectivity. Light gray dashed line is the CPL lidar attenuated backscatter profile. Dark gray solid line is CPL backscatter coefficient, and gray dashed line is the lidar-derived cumulative particulate optical depth.

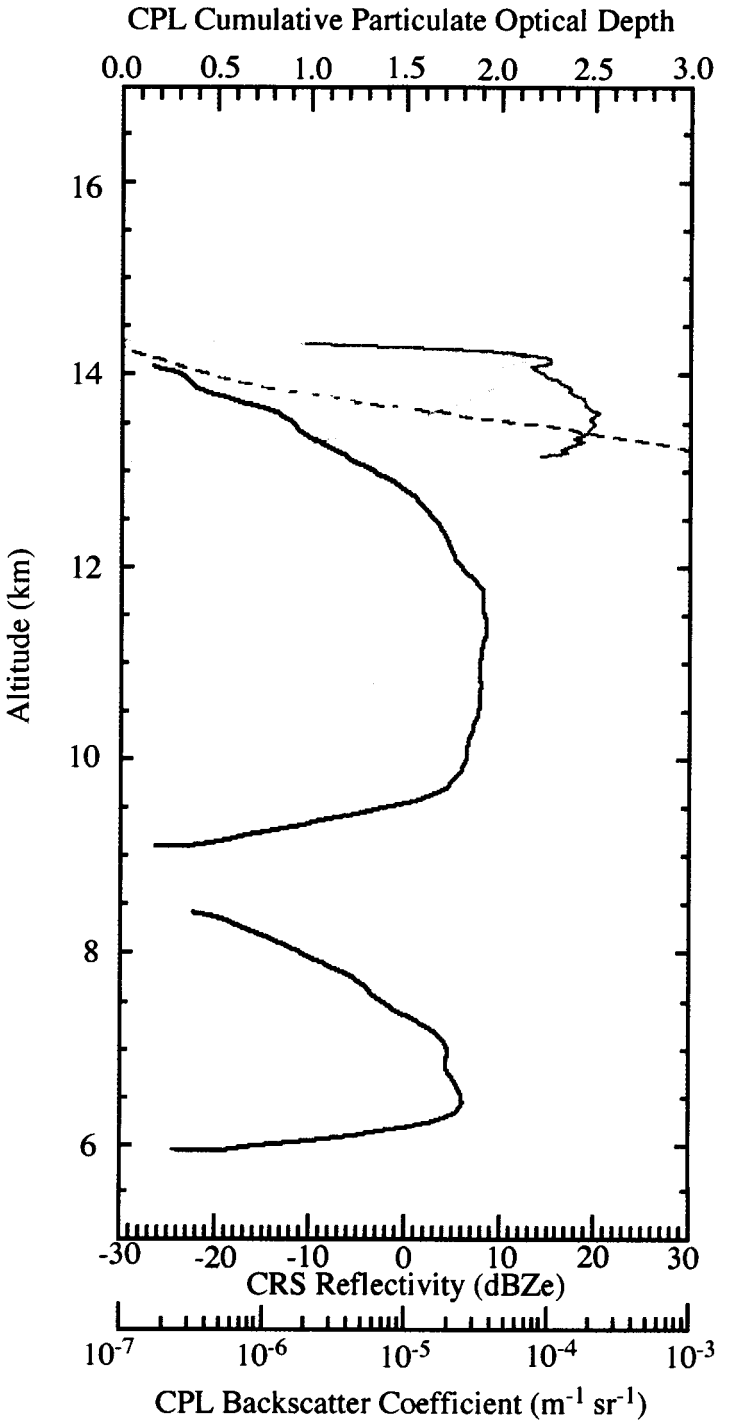

Figure 5: Profiles from 20:50:48 UTC, July 23, 2002. Solid black line is the CRS radar reflectivity. Light gray dashed line is the CPL lidar attenuated backscatter profile. Dark gray solid line is CPL backscatter coefficient, and gray dashed line is the lidar-derived cumulative particulate optical depth

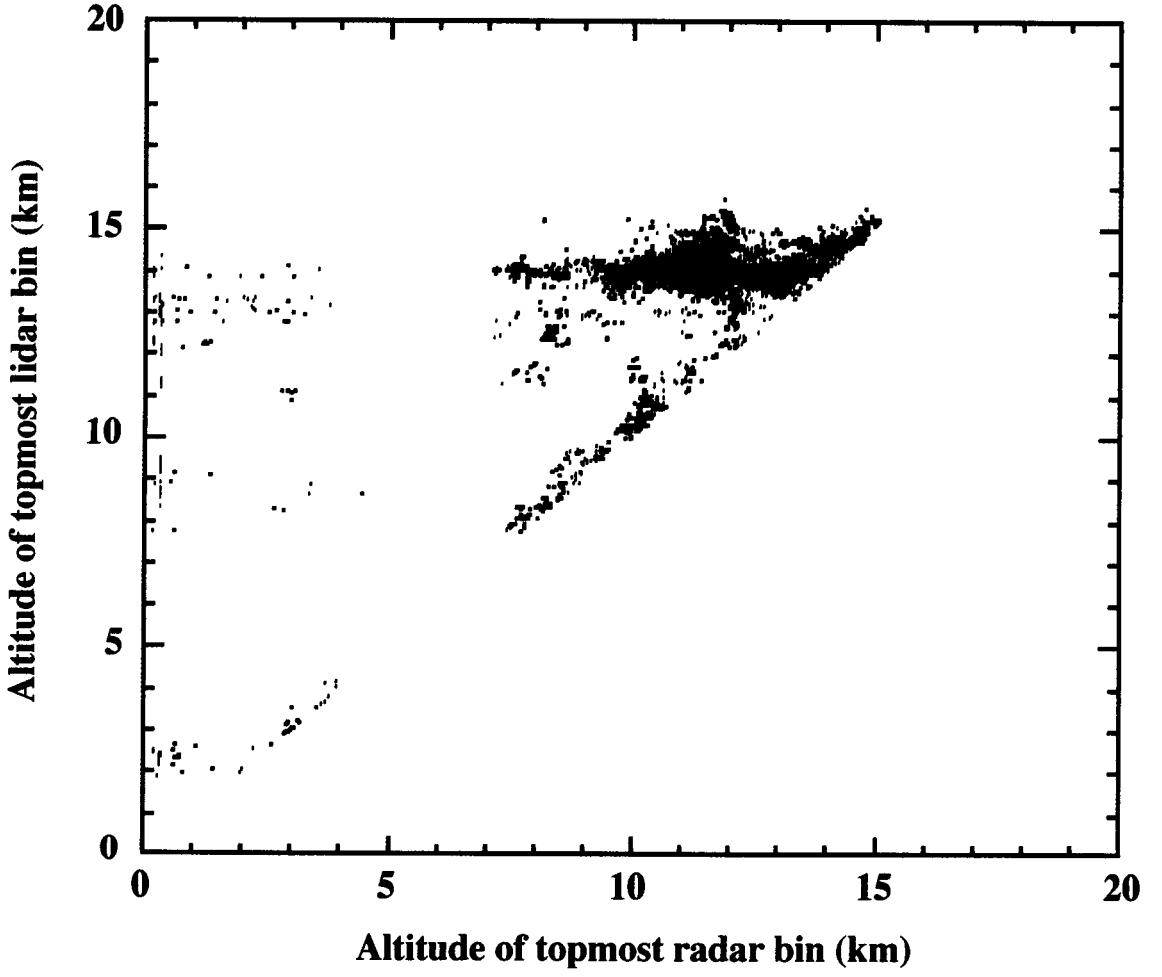

Figure 6: Comparison of topmost layer height, from July 23, 2002. The lidar consistently detects layer boundaries before the radar.

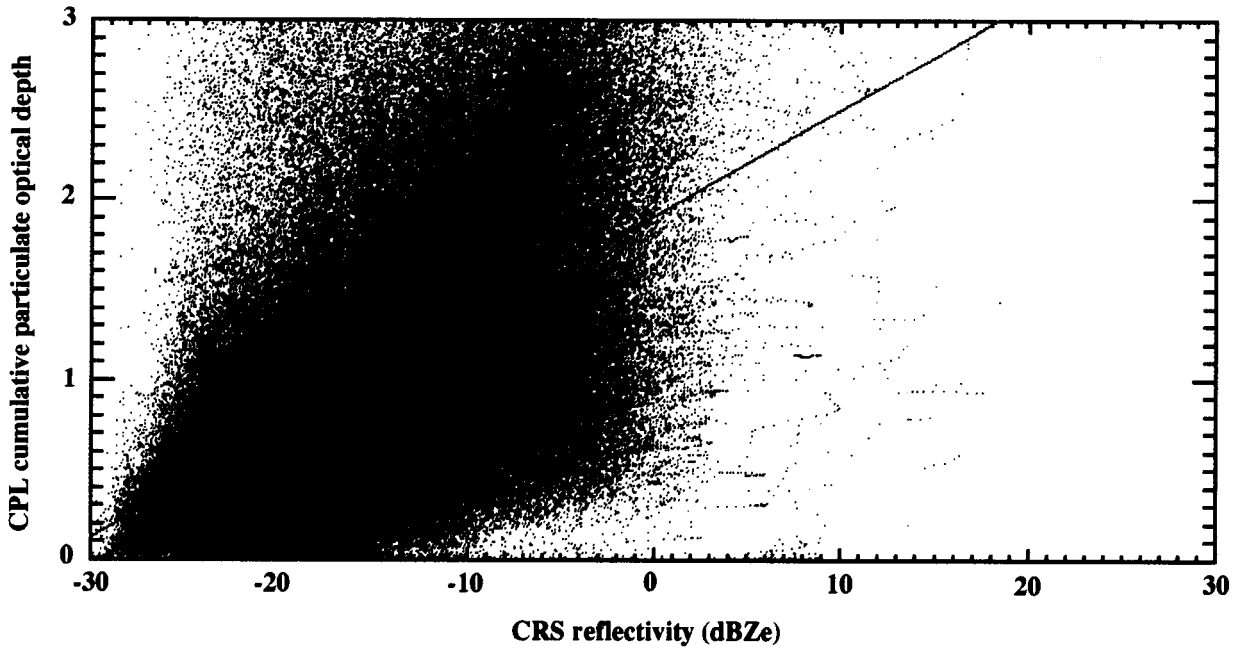

Figure 7: Scatterplot of radar reflectivity versus lidar-derived cumulative particulate optical depth, for July 23, 2002. Gray line overplotted is the best fit (χ^2) to the data.

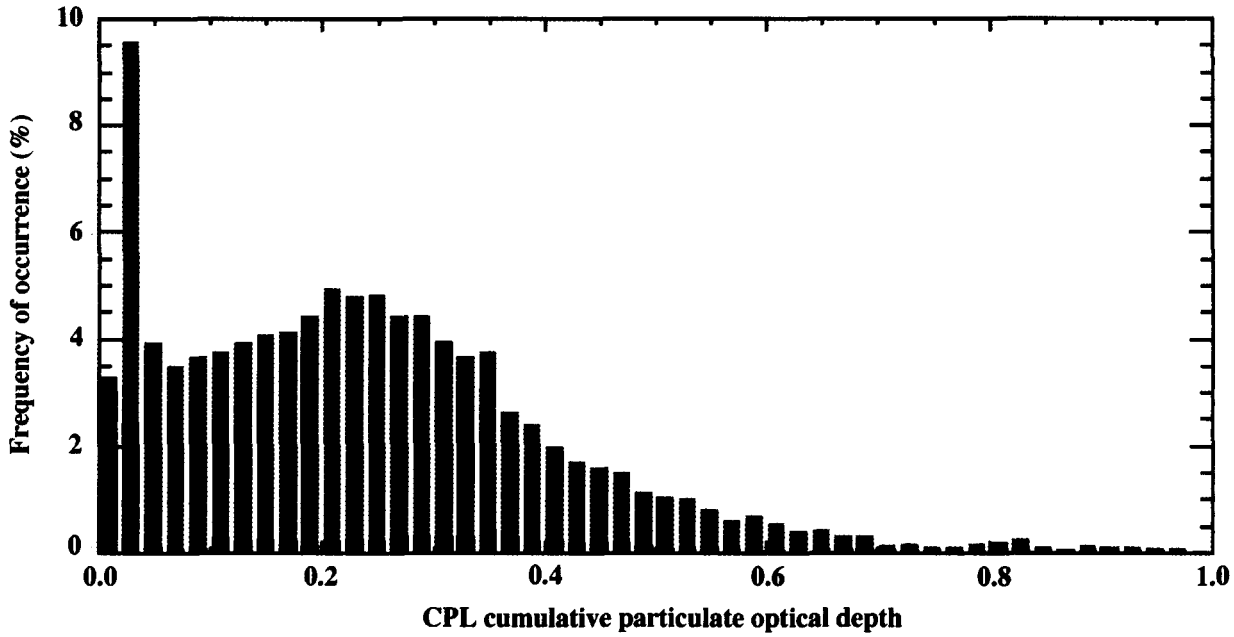

Figure 8: Occurrences of cumulative particulate optical depth derived from lidar measurements. Gray histogram shows all optical depths missed by the radar (e.g. optical depth down to the first detected radar bin). Overplotted in black is the optical depth missed when the radar senses nothing in an entire profile. In general, the lidar cumulative optical depth has to reach ~0.3 before the radar begins to detect signal.

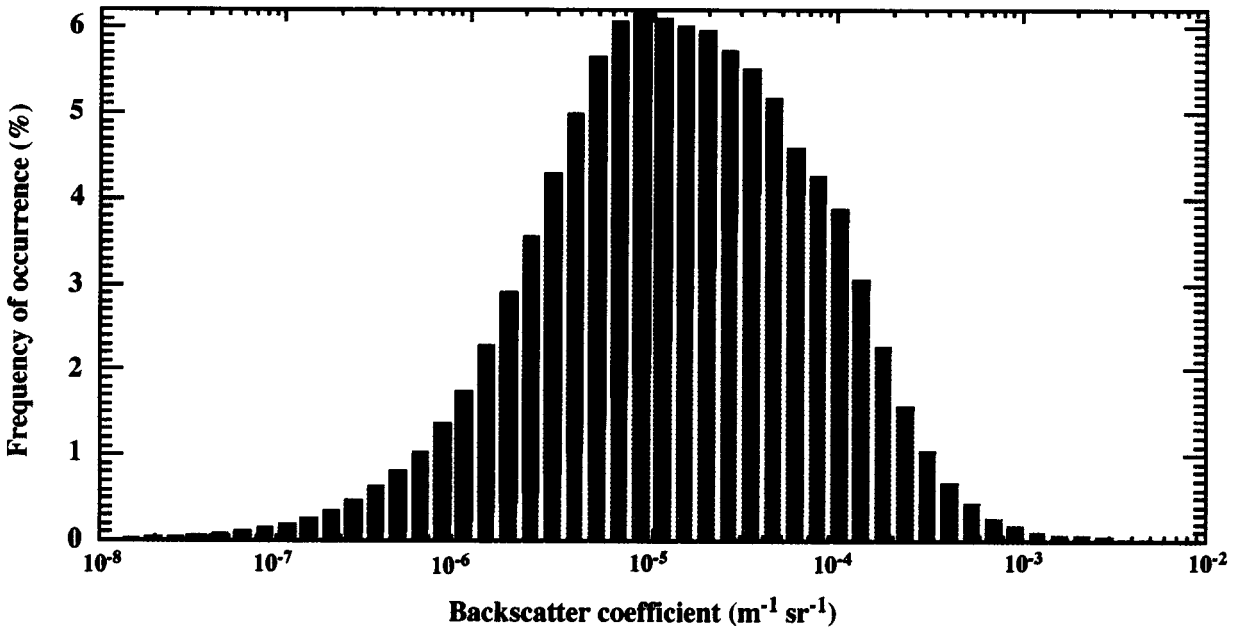

Figure 9: Distribution of backscatter coefficients from all lidar measurements within layers (black histogram). From July 23, 2002 data. Overplotted in gray is the subset detected by the lidar in regions where there was also valid radar signature (i.e., the instrument overlap).

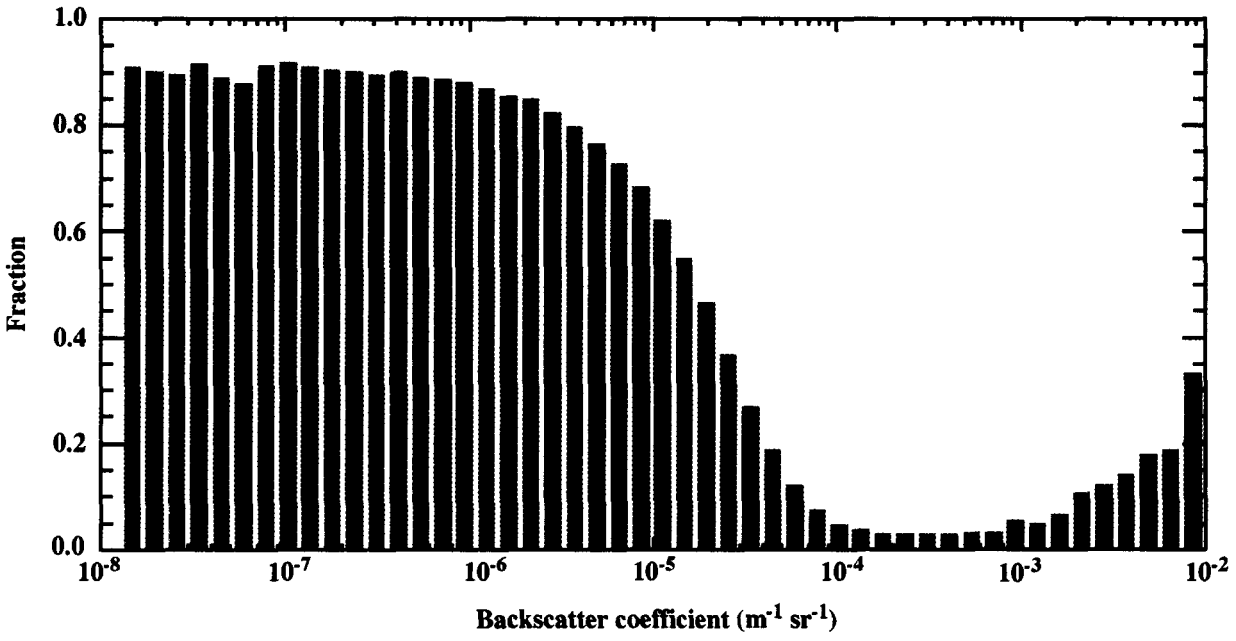

Figure 10: Distribution of backscatter coefficients from lidar in regions where the radar did not detect valid signal, July 23, 2002. This is a distribution of backscatter effectively missed by the radar, plotted as fraction of occurrences missed by the radar.

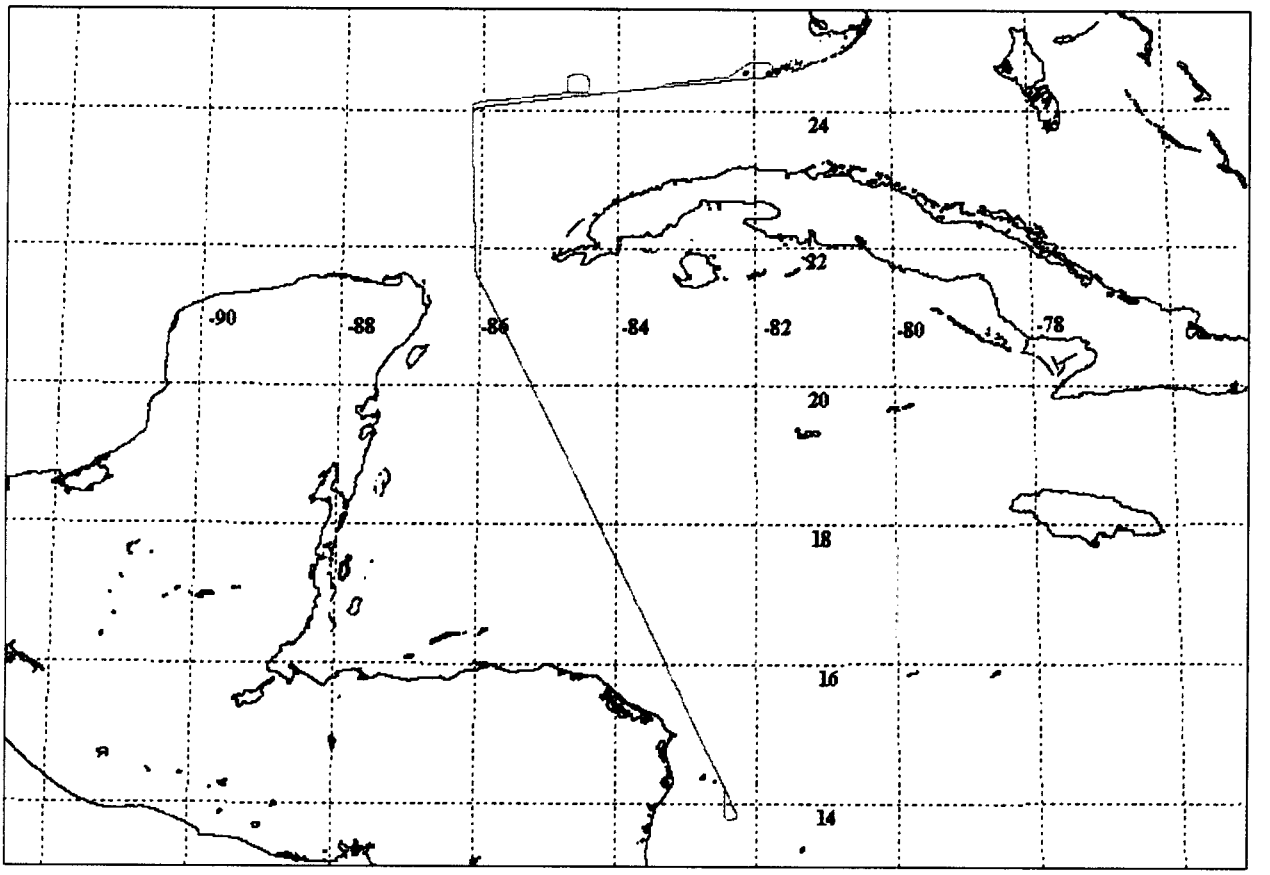

Figure 11: ER-2 flight track for July 26, 2002.

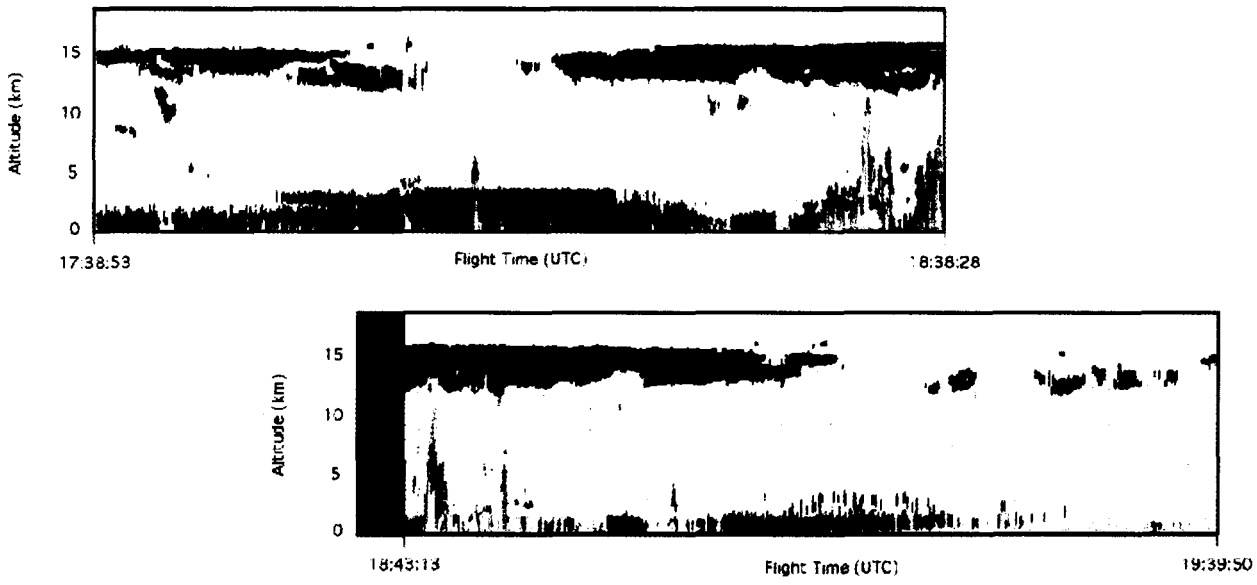

Figure 12: Composite image for July 26, 2002. Only the middle half of the flight is shown, as there was no radar signature in the early and later portions of the flight. The black region masks a 180-degree turn at the southern end of the flight track. Regions shaded in blue indicate lidar detection only, yellow indicates radar detection only, and green indicates both. Note that unlike the July 23 case, there is less overlap of the instruments in this example.

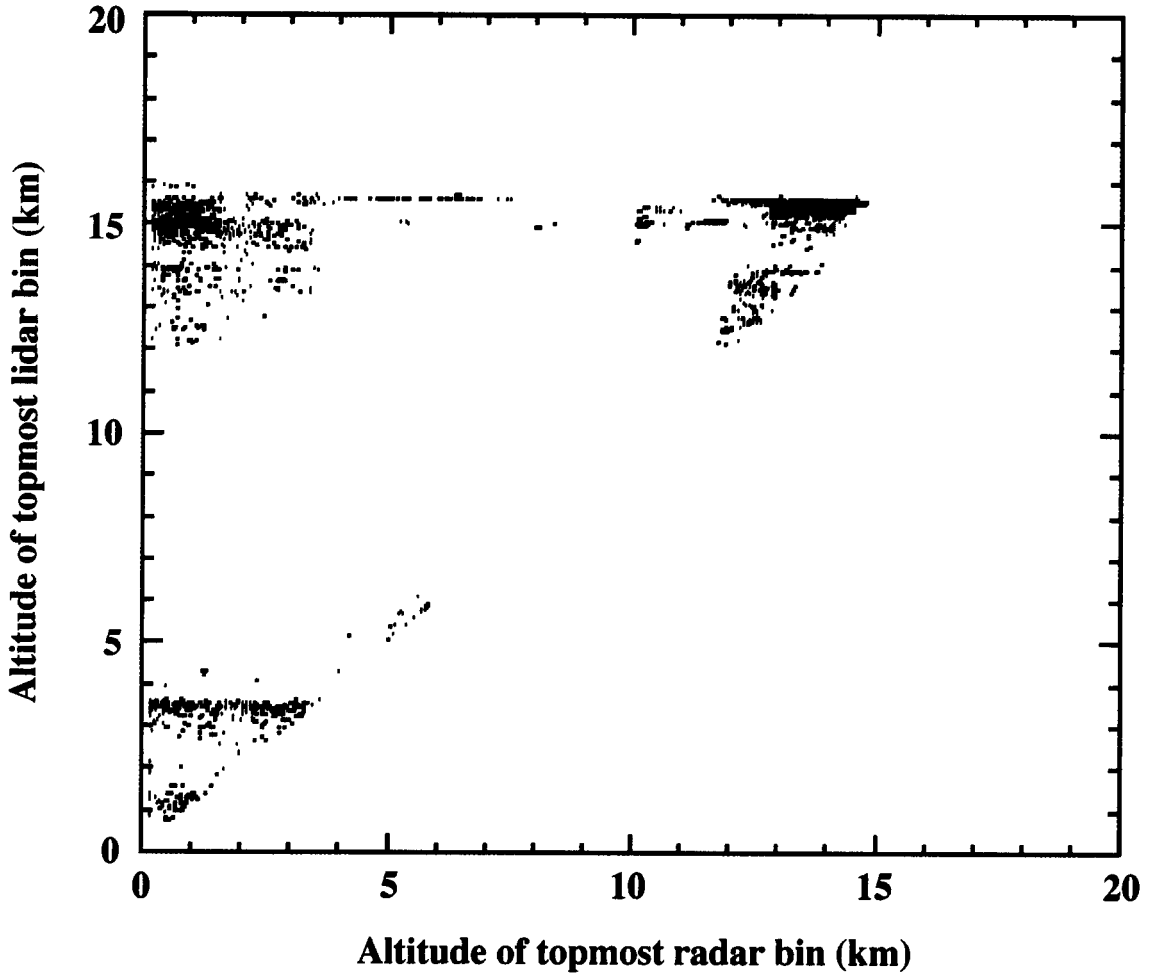

Figure 13: Comparison of topmost layer height, from July 26, 2002. Compare with Figure 6 for July 23.

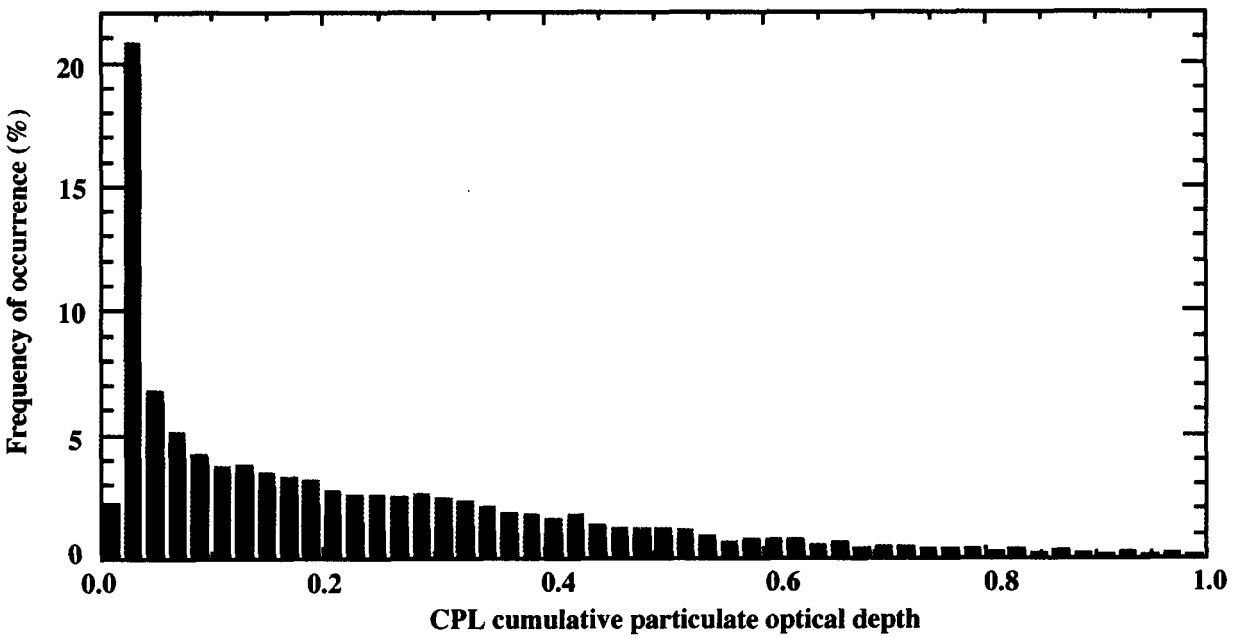

Figure 14: Occurrences of cumulative particulate optical depth derived from lidar measurements, July 26, 2002. Gray histogram shows all optical depths missed by the radar (e.g. optical depth down to the first detected radar bin). Overplotted in black is the optical depth missed when the radar senses nothing in an entire profile. Compare with Figure 8 for July 23.

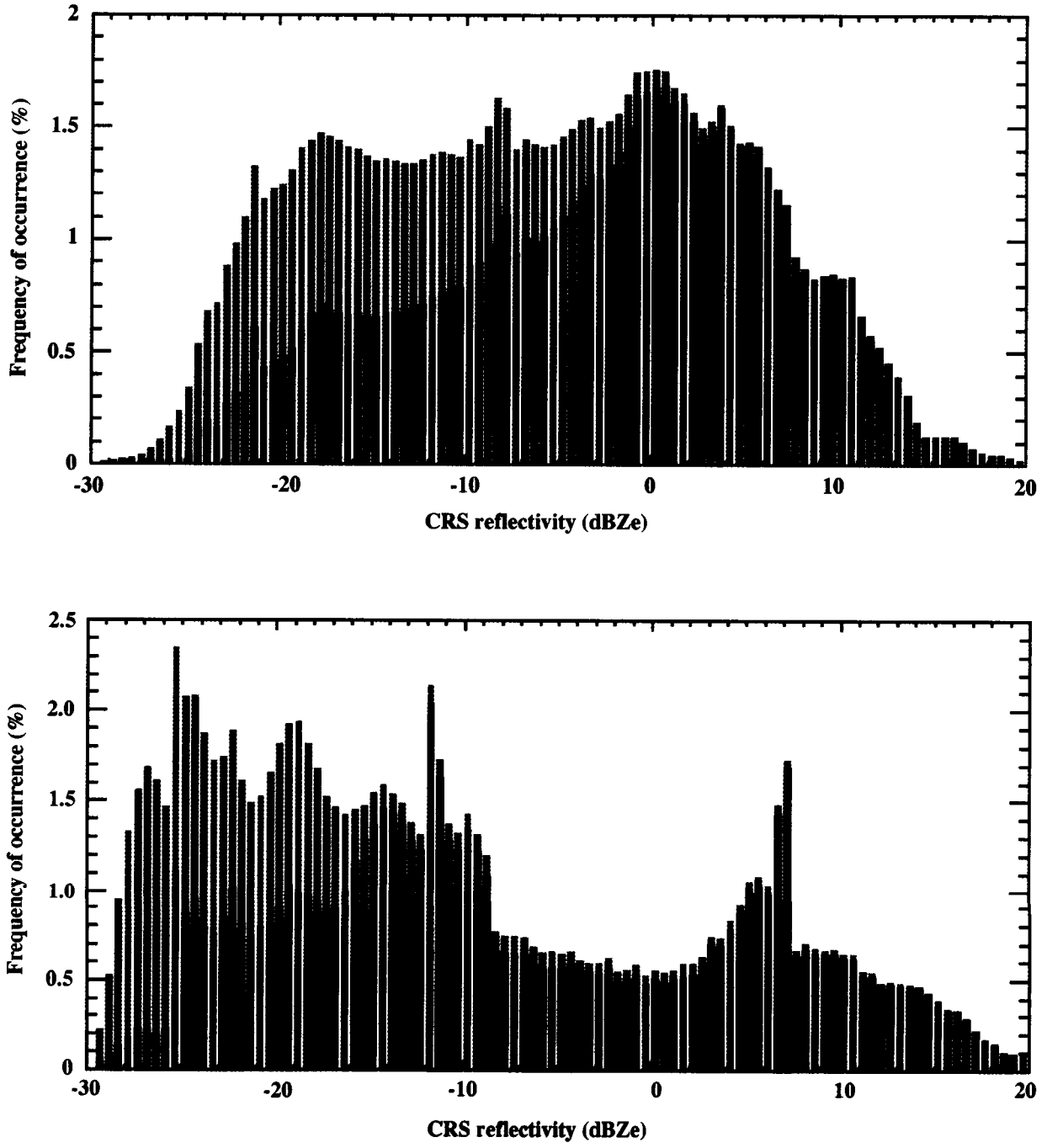

Figure 15: (top) Distribution of CRS radar reflectivity for July 23, 2002. (bottom) Same, for July 26, 2002. In each case, the gray histogram is all bins detected by the radar (including regions also sensed by the lidar). Overplotted in black is the subset of bins from regions where only the radar detected valid layer signature.

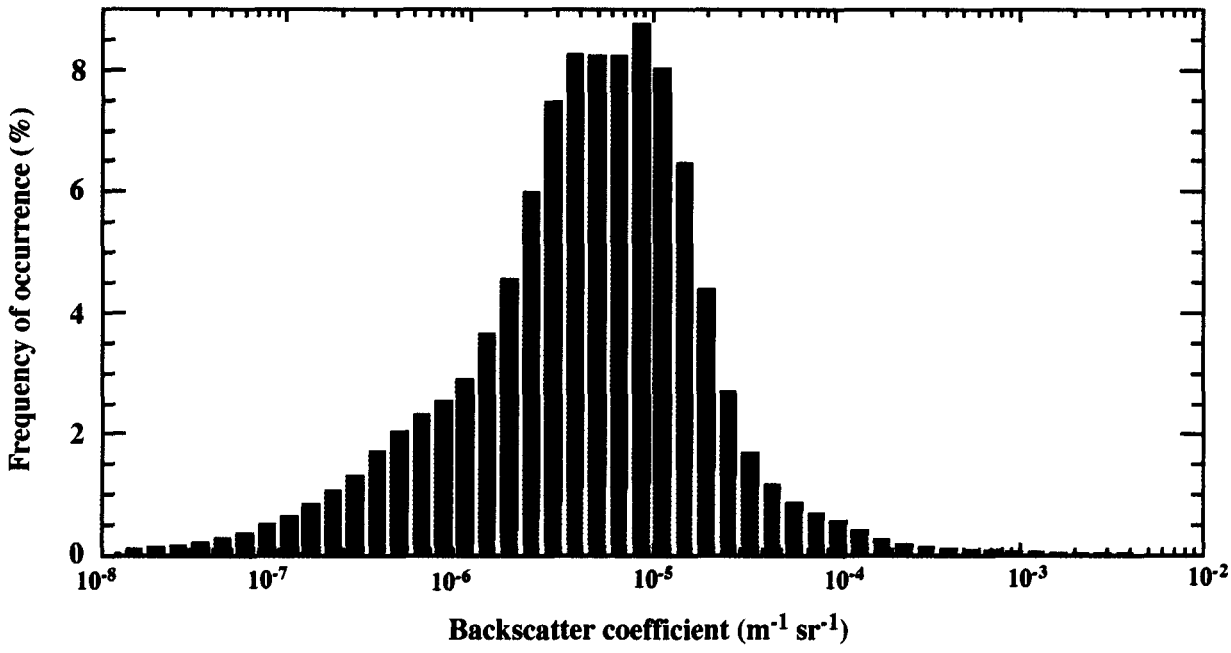

Figure 16: Distribution of backscatter coefficients from all lidar measurements within layers (black histogram). From July 26, 2002 data. Overplotted in gray is the subset detected by the lidar in regions where there was also valid radar signature (i.e., the instrument overlap). Compare with Figure 9 for July 23.

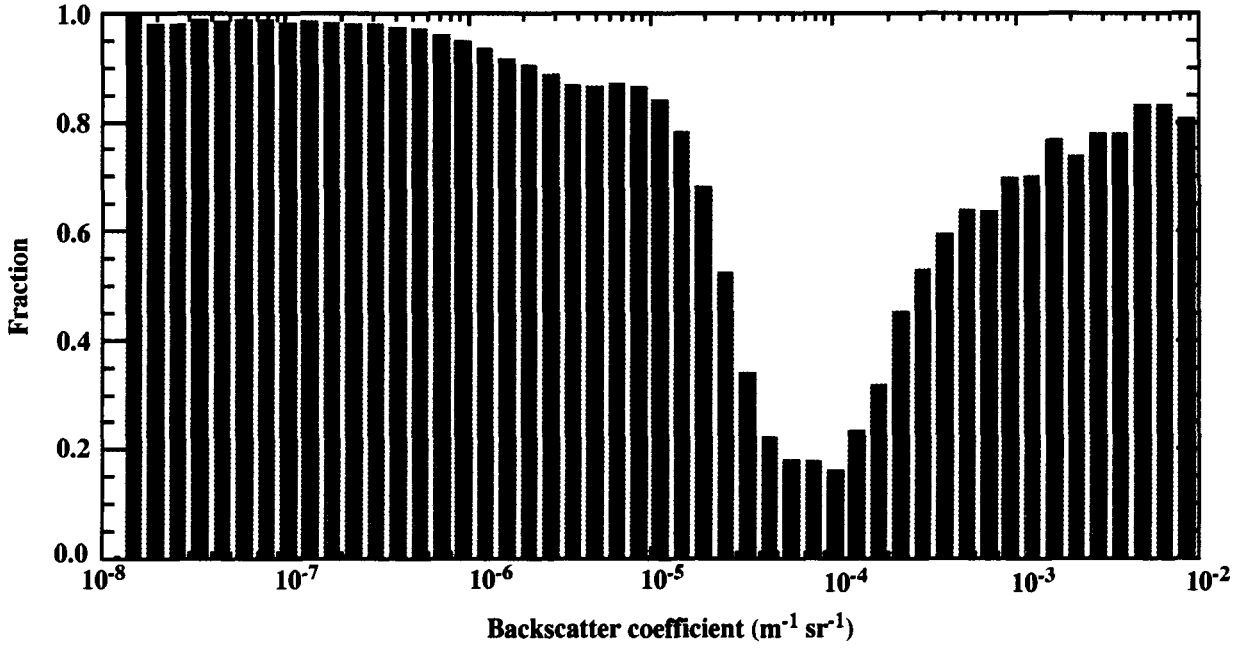

Figure 17: Distribution of backscatter coefficients from lidar in regions where the radar did not detect valid signal, July 26, 2002. This is a distribution of backscatter effectively missed by the radar, plotted as fraction of occurrences missed by the radar. Compare with Figure 10 for July 23.